Observation of entanglement spectrum signature for higher-order topology

Pengtao Lai[1], Yuanshuo Liu[1], Zhenhang Pu[2], Yugan Tang[1], Hui Liu[1], Weiyin Deng[2*], Hua Cheng[1*], Zhengyou Liu[2,3*], and Shuqi Chen[1,4,5*]

[1] *The Key Laboratory of Weak Light Nonlinear Photonics, Ministry of Education, School of Physics and TEDA Institute of Applied Physics, Nankai University, Tianjin 300071, China*

[2] *Key Laboratory of Artificial Micro- and Nanostructures of Ministry of Education and School of Physics and Technology, Wuhan University, Wuhan 430072, China*

[3] *Institute for Advanced Studies, Wuhan University, Wuhan 430072, China*

[4] *School of Materials Science and Engineering, Smart Sensing Interdisciplinary Science Center, Nankai University, Tianjin 300350, China*

[5] *The Collaborative Innovation Center of Extreme Optics, Shanxi University, Taiyuan 030006, China*

Bulk-boundary correspondence is crucial for understanding topological insulators, as it indicates that nontrivial bulk topology can be revealed from the boundary response. However, not all topological insulators exhibit conventional energy or frequency boundary responses despite possessing a nontrivial bulk topology, which challenges the experimental probing of bulk topology. In this work, we utilize the entanglement spectrum, rather than the energy or frequency spectrum, for experimentally probing the bulk topology. We verify the bulk-entanglement spectrum correspondence in an acoustic multipole topological insulator even without the frequency boundary response. Our work provides a novel paradigm for probing the bulk topology and opens new avenues for exploring topological materials.

entanglement spectrum, bulk-boundary correspondence, higher-order topology, phononic crystals

1   Introduction

Bulk-boundary correspondence (BBC), the nontrivial bulk topology can be revealed by the boundary response, which plays an important role in experimentally probing bulk topology [1-3]. Higher-order topological insulators (TIs) [4-7] and semimetals [8-12], which feature boundary states localized at the boundary of a boundary, extend the BBC. Multipole TI, a quintessential example of higher-order TI, has been realized in phononic crystals (PCs) [13-17], photonic crystals [18-20], and electric circuits [21,22]. To date, probing the bulk multipole moment relies on the observation of higher-order boundary modes in the energy or frequency spectrum, which, however, depend not only on the bulk multipole moment but also on the boundary moment [4]. Therefore, these energy or frequency boundary modes presence or not does not necessarily correspond to the bulk multipole moment [23-27], indicating a breakdown of BBC.

Entanglement entropy, which measures the quantum entanglement and nonlocal correlation, is a key concept in quantum information science [28]. Figure 1(a) illustrates a

---

*Corresponding authors (Weiyin Deng, email: dengwy@whu.edu.cn; Hua Cheng, email: hcheng@nankai.edu.cn; Zhengyou Liu, email: zyliu@whu.edu.cn; Shuqi Chen, email: schen@nankai.edu.cn)

maximally entangled two-qubit state, namely the Bell state [29], which underpins our understanding of quantum non-locality [30] and plays a crucial role in applications such as superdense coding [31] and quantum teleportation [32,33]. Similarly, the insulator can also be divided into two sub-systems, as shown in Figure 1(b) and (d). For the trivial insulator, which can slowly turn off the hopping and adia-batically transform into the atomic limit [34], the entangle-ment entropy between two subsystems is zero, as there is no coupling between two subsystems in the atomic limit. Thus, a nontrivial TI can be defined as an insulator having en-tanglement entropy that cannot be adiabatically tuned to zero. This information field concept offered new insights into the topological nature of systems [35-37].

Compared with the single-valued entanglement entropy S, the entanglement spectrum (ES), which is defined as the spectrum of the logarithm of the reduced density matrix or, equivalently, the eigenvalues of the correlation matrix (de-noted as $\{\varepsilon_n\}$) [38], captures key features of edge states [39-42]. The relationship between the entanglement entropy S and ES $\{\varepsilon_n\}$ is $S = -\sum_n [\varepsilon_n \log \varepsilon_n + (1-\varepsilon_n)\log(1-\varepsilon_n)]$. For nontrivial TIs, it has been proposed that the ES eigenvalues $\{\varepsilon_n\}$ cannot be adiabatically pushed to 0 or 1, which corre-sponds to zero entanglement entropy [43]. As such, the TIs exhibit the bulk-ES correspondence. In first-order TIs [44-47], such as Chern insulators, the spectral flow of edge states corresponds to a spectral flow in the ES, as depicted in Figure 1(c). The higher-order TIs, such as quadrupole TIs,

can give rise to the mid-gap states in the ES [48-50]. Re-cently, it has been found that the quadrupole TIs without corner states in the energy spectrum remain hosting the ES corner states [26]. However, despite some advances in measuring the ES [51] and entanglement entropy [52], the correspondence between higher-order topology and the ES remains to be demonstrated in experiments.

In this work, we measure the ES for experimentally probing the bulk topology and verify the bulk-ES corre-spondence in an acoustic multipole TI. We designed and fabricated three distinct PCs with nontrivial quadrupole moments. All these three PCs exhibit ES corner states, cor-responding to the nontrivial quadrupole moment. Never-theless, the frequency corner states only appear in the PC with nonzero corner charge. With boundary modifications, a phase transition of corner charge takes place, while the quadrupole moment remains nontrivial. In this case, the frequency corner modes vanish, whereas the ES corner modes persist, faithfully reflecting the nontrivial quadrupole moment. Both the experimental and simulated results con-firm the bulk-ES correspondence, rather than the conven-tional BBC, in the multipole TIs.

2   ES in the multipole TI

According to the classical electromagnetic theory of multi-pole moments, charge accumulation at the corner arises from two components: the first one is the edge polarization, which
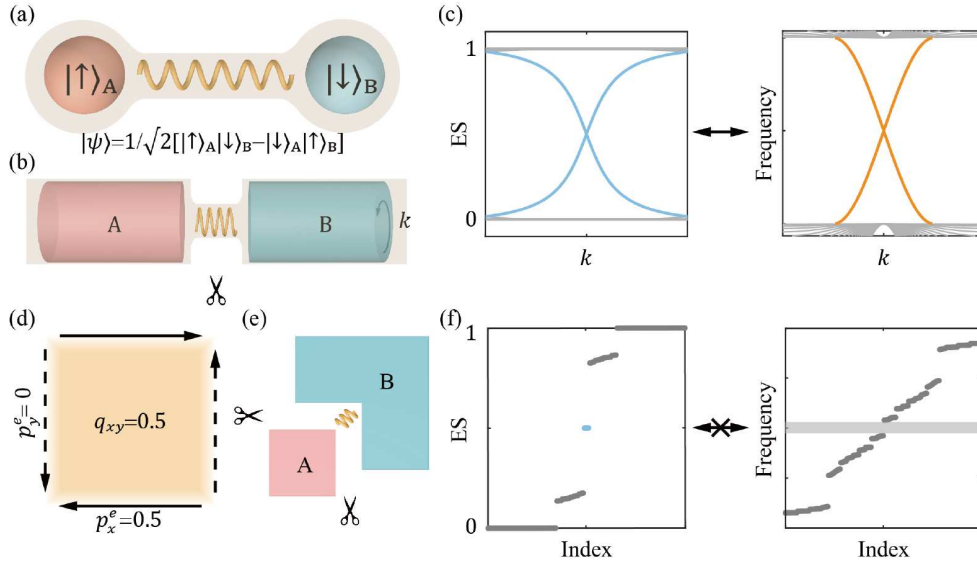
Figure 1 (Color online) Bulk-ES correspondence in TIs. (a) A maximally entangled two-qubit Bell state. The entanglement between two qubits is characterized by the entanglement entropy. (b) Real-space cut of first-order TI. The system, with the periodic boundary condition along one direction, is partitioned into two halves. (c) Correspondence between the ES (left panel) and the edge spectrum (right panel). (d) A special case with $\left(q_{xy}, p_x^e, p_y^e\right)=$ (0.5,0.5,0). despite the quadrupole moment being nontrivial, no frequency corner modes appear ($Q^c=0$). (e) Real-space cut for multipole TI. The quadrupole moment is revealed by the 1/2-in-gap states in the ES. (f) The ES faithfully reflects the nontrivial bulk quadrupole moment even when frequency corner states are absent.

is a pure surface effect and independent of the bulk moment; the other one is the bulk quadrupole moment [4]. The total corner charge is

$$Q^c = p_x^e + p_y^e - q_{xy}, \tag{1}$$

where p_x^e and p_y^e are edge polarizations in the x and y directions, respectively. Due to the contribution of edge polarization, the frequency corner state does not directly reflect the quadrupole moment. Figure 1(d) presents a special case with (q_{xy}, p_x^e, p_y^e)=(0.5, 0.5, 0). In this case, despite the quadrupole moment being nontrivial, no frequency corner modes appear, indicating a breakdown of the BBC.

However, since ES depends solely on the bulk ground states, it is suitable for identifying the quadrupole moment. As shown in Figure 1(e), the whole system is divided into two subsystems, A and B, where A is a quarter of the system and B is the complement of A (for an alternative partition method, see Supplementary Note 1). The correlation matrix of subsystem A, with $L_x \times L_y$ unit cells, is given by

$$C_{ij}(A) = \frac{1}{L_x L_y} \sum_k e^{ik(i-j)} \widehat{P}_k^*, \tag{2}$$

where i and j denote the lattice sites within the subsystem A, and $\widehat{P}_k$ is the projection operator of the ground states and $\widehat{P}_k^*$ is its conjugate [43]. The ES exhibits protected 1/2-in-gap modes for the quadrupole nontrivial insulators [49]. Therefore, the ES provides a more accurate representation of bulk topology than the edge mode spectrum, as illustrated in Figure 1(f).

3   Design of PC

To validate the bulk-ES correspondence, we designed the PC model illustrated in Figure 2(a). The unit cell of the airborne PCs consists of four identical cuboid air cavities with dimensions: height h=24 mm, width r=12 mm, and connected by cross-linked tubes. The lattice constant is a=88.5 mm. The red and blue tubes, with heights h_1=5.5 mm and h_2=6 mm, serve as the negative and positive couplings, respectively (see Supplementary Note 3 for more details about the design of couplings). All tubes are connected to the cavities at a distance of d=8 mm from the top and bottom surfaces of the cavities. The width of the intra-cell coupling tubes is w=2.2 mm, while the widths of the inter-cell coupling tubes in the x and y directions are denoted as w_x and w_y, respectively (for more details about the model Hamiltonian, see Supplementary Note 2). Two momentum-space glide symmetries $M_x^g = \tau_3 \otimes \sigma_1$ and $M_y^g = \tau_1 \otimes \sigma_0$, where τ_0 (σ_0) is the 2×2 identity matrix, τ_i and σ_i with i=1,2,3 are Pauli matrices, quantize the polarization and quadrupole moment to 0 or 0.5 [27].

Figure 2(b) presents the phase diagram characterized by the (q_{xy}, p_x^e, p_y^e) as a function of the inter-cell coupling tube widths w_x and w_y. The second bulk band gap closes at the blue line, and the quadrupole moment transitions from 0 to 0.5 as the widths w_x and w_y increase. At the dark grey lines, where the widths of inter-cell and intra-cell coupling tubes coincide, the edge band gap closes and edge polarization undergoes a phase transition (see Supplementary Note 4). According to eq. (1), frequency corner modes appear only in the green region. In the orange and yellow regions, despite a nontrivial quadrupole moment, frequency corner modes are absent, indicating a breakdown of BBC.

The experimental setup is illustrated in Figure 2(c). The sound source is placed at the center of the sample to excite the bulk states and probe the acoustic pressure in each cavity located away from the boundaries. The pump-probe response is collected by the vector network analyzer (Keysight E5061B). After the Fourier transformation, the real-space pump-probe response is converted to the momentum space. At the resonance frequency, the Bloch ground states can be obtained via the singular value decomposition of the momentum-space response tensor (for more details, see Supplementary Note 6). With the extracted wavefunction, we can obtain the correlation matrix C(A) and the ES from eq. (2).

4   Bulk-ES correspondence

4.1   Bulk-ES correspondence without frequency corner modes

To validate the correspondence between the quadrupole moment and the ES in experiment, we first designed a PC with dimensions w_x=4.5 mm and w_y=1 mm, which corresponds to the yellow region in Figure 2(b). As shown in Figure 2(d), a PC, comprising 12×12 unit cells, was fabricated by the 3D printing technology. Figure 2(e) displays the calculated nested Wannier bands for the lowest two bands, derived from phononic wavefunctions obtained using the COMSOL Multiphysics solver, confirming the nontrivial quadrupole moment. Figure 2(f) shows the simulated eigenfrequency spectra of the PC, where the color represents the degree of localization at four corners, defined as $Col = \sum_{r \in c} |\psi_e(r)|^2$, with c denoting the four corners of the sample. It can be seen from Figure 2(f) that frequency corner states neither appear within the band gap nor merge into the bulk bands to form bound states in the continuum. To confirm the absence of frequency corner states, we probed the response spectrum with local excitations at corner (C_1), edge (C_2), and bulk (C_3), and normalized the data by the maximum value. As shown in Figure 2(g), the response spectrum at the corner overlaps with that at the edge, and no resonant peaks
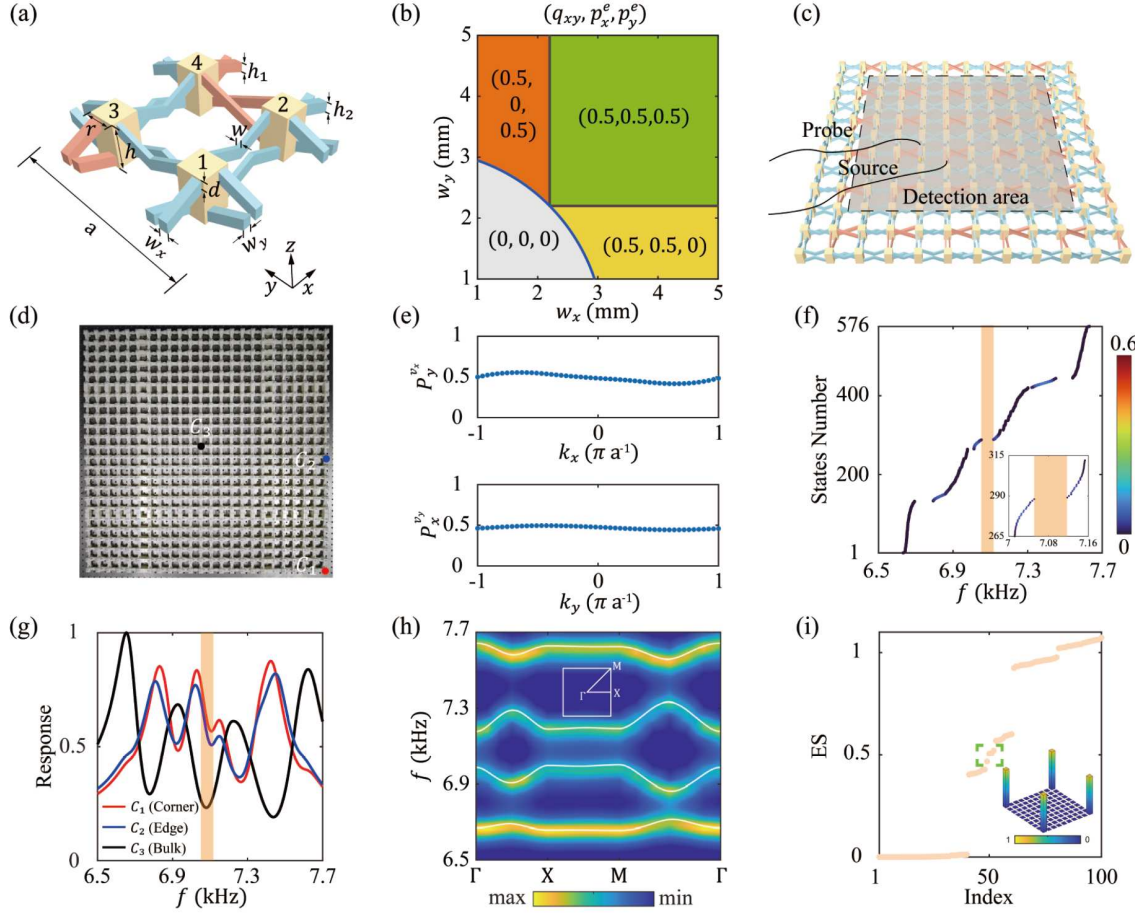
Figure 2 (Color online) Experimental validation of the bulk-ES correspondence. (a) Unit cell of the PC. All colored solid shapes represent air. Four acoustic resonators (yellow cuboids) are connected by red (negative) and blue (positive) coupling tubes. (b) Phase diagram characterized by the quadrupole moment q_{xy} and edge polarizations p_x^e and p_y^e in the w_x-w_y plane. The blue and dark grey lines indicate the closing of bulk and edge band gaps, respectively. (c) Schematic of the measurement of the ES via the pump-probe procedure. (d) Photograph of the fabricated PC sample with parameters w_x=4.5 mm and w_y=1 mm. (e) Calculation of the nested Wannier bands $P_y^{v_x}(k_x)$ and $P_x^{v_y}(k_y)$, derived from simulated wavefunctions, confirming q_{xy}=0.5. (f) Simulated eigenfrequency spectrum. The color denotes the degree of localization at corners. Inset: enlarged view of the band gap, showing that no corner states emerge within the gap. (g) Measured response spectra at C_1 (corner), C_2 (edge), and C_3 (bulk). (h) Measured (color map) and simulated (white lines) bulk band dispersions. (i) Measured ES. There exist four 1/2-in-gap modes, which are consistent with a nontrivial quadrupole moment. The inset illustrates the field distributions of these corner-localized modes.

appear in the band gap. Consequently, frequency corner modes are absent, making it impossible to characterize the nontrivial bulk topology by them.

Figure 2(h) illustrates the measured band dispersion, which is also obtained from the momentum-space response function (for more details, see Supplementary Note 6). The measured dispersions agree well with the simulated results (white lines). Following the procedure introduced above, we measured the ES of the PC. As shown in Figure 2(i), the ES exhibits four 1/2-in-gap modes, consistent with a nontrivial quadrupole moment. The inset displays the field distribution of these mid-gap modes, defined as $W(j) = \sum_n |\phi_n(j)|^2$, where $\phi_n(j)$ is the n-th eigenstate of the correlation matrix and the summation is performed over the mid-gap states. These modes are mainly localized at four corners. Ideally, the

ES should range from 0 to 1, but in our experimental results, it slightly exceeds 1, attributed to unavoidable air loss and the finite size of the PC.

4.2   Bulk-ES correspondence with frequency corner modes

The second PC, with dimensions w_x=4 mm and w_y=3.5 mm, is located in the green region in Figure 2(b). Following the same methodology introduced above, we measured the bulk band dispersions and ES. As shown in Figure 3(a), the measured bulk band dispersions agree well with the simulated result (white lines). The nested Wannier bands, calculated from the simulation results and presented in Figure 3(b), confirm the nontrivial quadrupole moment. Figure 3(c) displays the simulated eigenfrequency spectrum, and four
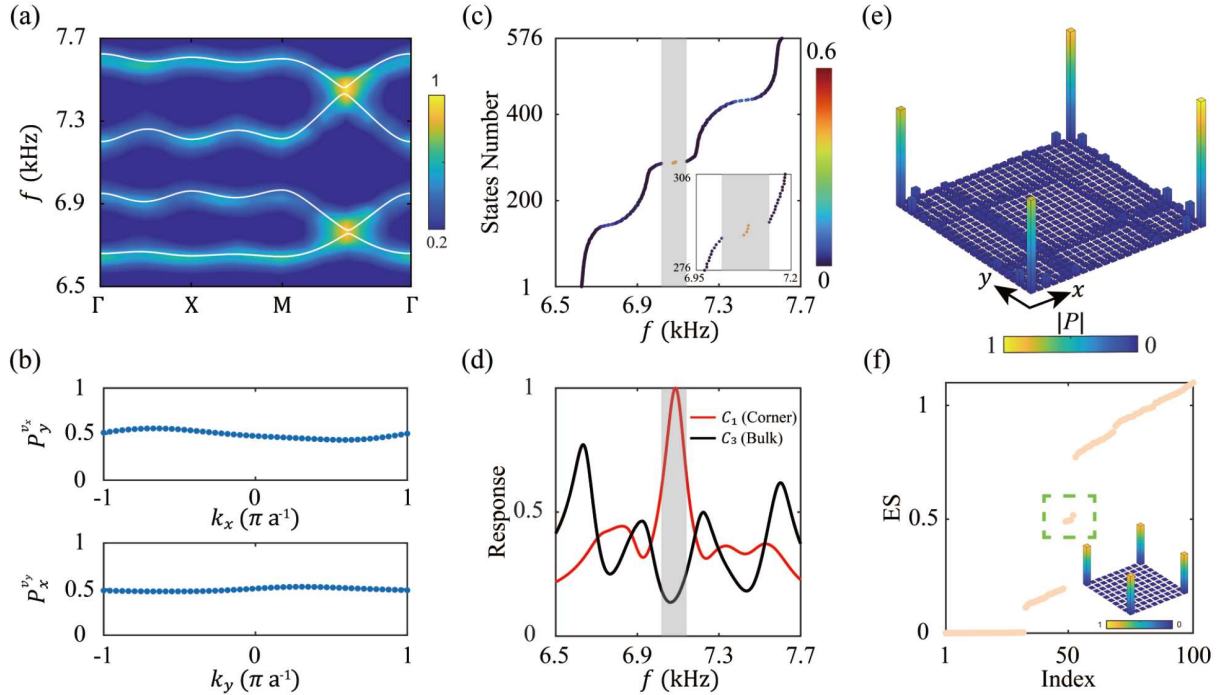
Figure 3 (Color online) Observation of corner states in the frequency and ES, simultaneously. (a) Measured (color map) and simulated (white lines) bulk band dispersions of PC with w_x=4 mm and w_y=3.5 mm. (b) Calculation of the nested Wannier bands, confirming the nontrivial quadrupole moment. (c) Simulated eigenfrequency spectrum. There exist four corner states at the mid-gap. Inset: enlarged view of the corner states. (d) Measured response spectra at C_1 (corner) and C_3 (bulk). (e) Measured pressure field distribution at 7.09 kHz, illustrating the presence of corner states. (f) Measured ES. There exist four 1/2-in-gap modes, which are consistent with a nontrivial quadrupole moment. The inset displays the field distribution of these modes.

corner modes appear in the mid-gap, which is consistent with the nontrivial corner charge. The inset displays that the four corner modes appear around 7.09 kHz. In Figure 3(d), the red and black lines represent the measured broadband response spectra at the corner (C_1) and bulk (C_3), respectively. Four resonance peaks in the bulk response correspond to four bulk bands. A bulk band gap is clearly observed, and the corner response exhibits a resonant peak at around 7.09 kHz within the band gap, which agrees well with the simulation result in Figure 3(c). Figure 3(e) shows the measured field distribution at the peak frequency of the corner mode, which demonstrates strong field confinement at four corners. Slight variations in field intensity at four corners are attributed to fabrication imperfections. The measured ES, shown in Figure 3(f), features four 1/2-in-gap modes, consistent with the nontrivial quadrupole moment shown in Figure 3(b). The field distribution of four 1/2-in-gap modes is shown in the inset, where they are localized at the four corners. Therefore, both the frequency corner modes and the ES can characterize the nontrivial bulk topology of this phase.

4.3 Disappearance of the frequency corner modes via boundary modifications

These examples illustrate the correspondence between the nontrivial bulk topology and 1/2-in-gap modes in the ES.

Notably, since edge polarization is a pure surface effect, it is possible to induce a phase transition by modifying the boundary without altering the bulk. As the edge polarization changes, frequency corner states vanish, even though the quadrupole moment remains nontrivial. In contrast, 1/2-in-gap modes in the ES depend solely on the bulk topology and persist as long as the quadrupole moment is nontrivial.

To further illustrate this phenomenon, we designed the third PC. Starting from the second PC, we modified the width l_y of the intra-cell coupling tubes at the boundary, as highlighted in red in Figure 4(a), while leaving the bulk coupling tubes unchanged. As shown in Figure 4(b), an edge band inversion takes place upon increasing the width l_y, and the edge polarization p_y^e transitions at the same time. Notably, the bulk band gap does not close throughout this process, ensuring the quadrupole moment remains nontrivial (see Supplementary Note 4). As the edge polarization changes while the quadrupole moment remains invariant, the corner charge transitions from 0.5 to 0. Figure 4(c) presents the open boundary energy spectrum for l_y=4.5 mm, revealing the absence of corner modes in the band gap. Experimental measurements of the broadband response of acoustic pressure at corner, edge, and bulk are shown in Figure 4(e). Consistent with the simulations, no resonant pressure peaks are observed at the corner within the band gap. However, as the quadrupole moment remains nontrivial, four 1/2-in-gap
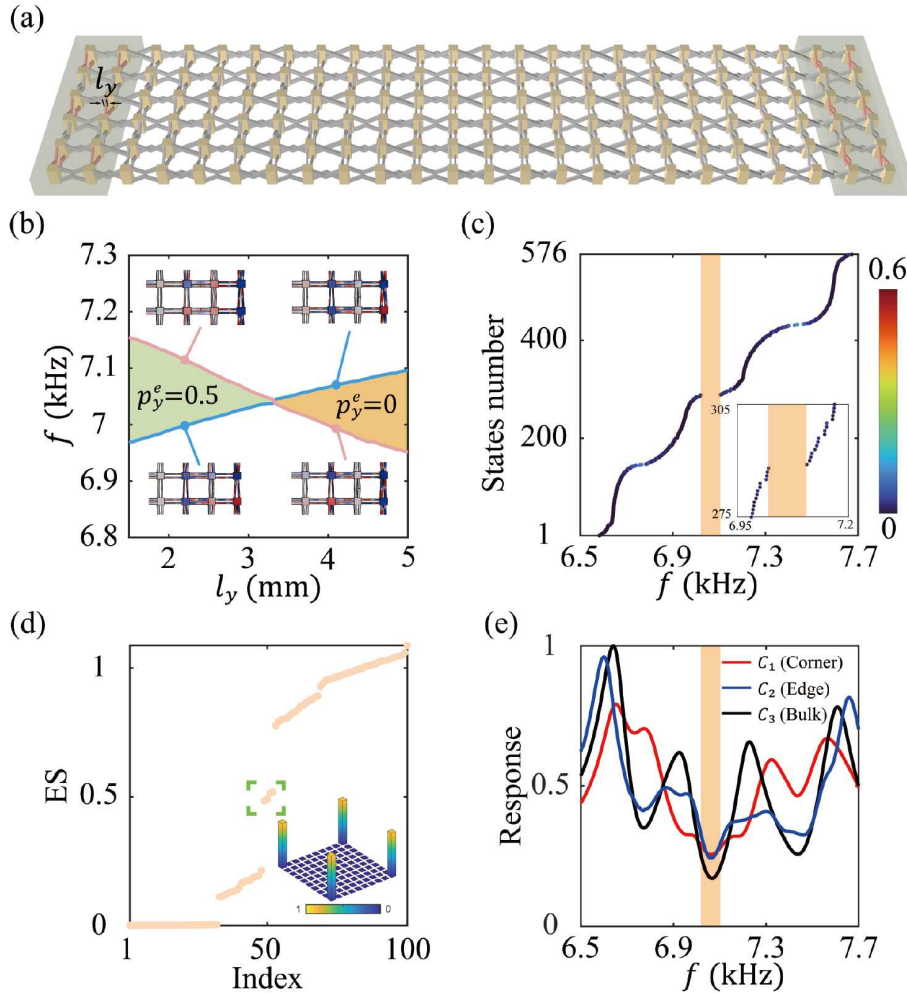
Figure 4 (Color online) Control the appearance of frequency corner states by adjusting the boundary modifications. (a) Schematic of the PC with modified intra-cell coupling tubes, which are highlighted in red. The width of the modified coupling tube is denoted as l_y. (b) Topological phase transition of edge polarization p_y^e. With increasing l_y, an edge band inversion takes place and the edge polarization p_y^e transitions at the same time. (c) Simulated eigenfrequency spectrum for l_y=4.5 mm. As shown in the inset, no corner states appear in the band gap after the phase transition. (d) Measured ES. Four mid-gap corner states correspond to the nontrivial quadrupole moment. (e) Measured response spectra at C_1 (corner), C_2 (edge), and C_3 (bulk), confirming the absence of frequency corner states.

modes can still be clearly observed in the experimental ES, as demonstrated in Figure 4(d), and the field distribution of these modes is shown in the inset. As the edge polarization is a surface effect and is susceptible to the modification of boundary, the entanglement spectrum is a more reliable indicator of bulk topological phase than the frequency corner modes.

5   Discussion

In conclusion, we have experimentally demonstrated the bulk-ES correspondence in multipole insulators. Traditionally, the experimental characterization of a nontrivial quadrupole moment has relied on the observation of frequency corner states. However, our results show that, despite a nontrivial bulk topology (quadrupole moment), the fre-

quency boundary response (corner states) may vanish, indicating a breakdown of the conventional BBC. Furthermore, edge polarizations are sensitive to boundary modifications, making the frequency corner state an unreliable indicator of bulk topology. To overcome this limitation, we propose that the experimental ES, which depends solely on the bulk ground states, provides a more robust and accurate method for probing bulk multipole topology.

Notably, this correspondence can also be extended to multipole topological semimetals, highlighting the broad applicability of ES in characterizing the topology of electric multipole moments (see Supplementary Note 8). Furthermore, the bulk-ES correspondence doesn't rely on a direct band gap; even if the chiral symmetry is broken and corner states merge into the bulk bands, the correspondence remains valid (see Supplementary Note 9). Beyond multipole TIs, the bulk-ES correspondence provides a unified framework for

diagnosing bulk topology, including both fragile [46] and stable topologies [47], and has potential applications in other topologies [53-55] and many-body [56,57] systems.

Conflict of interest   The authors declare that they have no conflict of interest.

Supporting Information

The supporting information is available online at http://phys.scichina.com and https://link.springer.com. The supporting materials are published as submitted, without typesetting or editing. The responsibility for scientific accuracy and content remains entirely with the authors.

1   C. W. Peterson, T. Li, W. A. Benalcazar, T. L. Hughes, and G. Bahl, Science **368**, 1114 (2020).

2   Z. Q. Jiao, S. Longhi, X. W. Wang, J. Gao, W. H. Zhou, Y. Wang, Y. X. Fu, L. Wang, R. J. Ren, L. F. Qiao, et al., Phys. Rev. Lett. **127**, 147401 (2021).

3   B. Xie, R. Huang, S. Jia, Z. Lin, J. Hu, Y. Jiang, S. Ma, P. Zhan, M. Lu, Z. Wang, et al., Nat. Commun. **14**, 7347 (2023).

4   W. A. Benalcazar, B. A. Bernevig, and T. L. Hughes, Science **357**, 61 (2017).

5   W. A. Benalcazar, T. Li, and T. L. Hughes, Phys. Rev. B **99**, 245151 (2019).

6   F. Schindler, A. M. Cook, M. G. Vergniory, Z. Wang, S. S. P. Parkin, B. A. Bernevig, and T. Neupert, Sci. Adv. **4**, eaat0346 (2018).

7   B. Xie, H. X. Wang, X. Zhang, P. Zhan, J. H. Jiang, M. Lu, and Y. Chen, Nat. Rev. Phys. **3**, 520 (2021).

8   M. Lin, and T. L. Hughes, Phys. Rev. B **98**, 241103 (2018).

9   S. A. A. Ghorashi, T. Li, and T. L. Hughes, Phys. Rev. Lett. **125**, 266804 (2020).

10   H. X. Wang, Z. K. Lin, B. Jiang, G. Y. Guo, and J. H. Jiang, Phys. Rev. Lett. **125**, 146401 (2020).

11   Q. Ma, Z. Pu, L. Ye, J. Lu, X. Huang, M. Ke, H. He, W. Deng, and Z. Liu, Phys. Rev. Lett. **132**, 066601 (2024).

12   Y. Qiao, F. Wang, H. Wang, Z. Tao, Z. Jiang, Z. Liu, S. Cho, F. Zhang, Q. Meng, W. Xia, et al., Sci. China-Phys. Mech. Astron. **67**, 247411 (2024).

13   M. Serra-Garcia, V. Peri, R. Süsstrunk, O. R. Bilal, T. Larsen, L. G. Villanueva, and S. D. Huber, Nature **555**, 342 (2018).

14   X. Ni, M. Li, M. Weiner, A. Alù, and A. B. Khanikaev, Nat. Commun. **11**, 2108 (2020).

15   H. Xue, Y. Ge, H. X. Sun, Q. Wang, D. Jia, Y. J. Guan, S. Q. Yuan, Y. Chong, and B. Zhang, Nat. Commun. **11**, 2442 (2020).

16   W. Zhu, W. Deng, Y. Liu, J. Lu, H. X. Wang, Z. K. Lin, X. Huang, J. H. Jiang, and Z. Liu, Rep. Prog. Phys. **86**, 106501 (2023).

17   Y. Wang, B. Liang, and J. Cheng, Sci. China-Phys. Mech. Astron. **67**, 224311 (2024).

18   B. Y. Xie, G. X. Su, H. F. Wang, H. Su, X. P. Shen, P. Zhan, M. H. Lu, Z. L. Wang, and Y. F. Chen, Phys. Rev. Lett. **122**, 233903 (2019).

19   S. Mittal, V. V. Orre, G. Zhu, M. A. Gorlach, A. Poddubny, and M. Hafezi, Nat. Photon. **13**, 692 (2019).

20   L. He, Z. Addison, E. J. Mele, and B. Zhen, Nat. Commun. **11**, 3119 (2020).

21   C. W. Peterson, W. A. Benalcazar, T. L. Hughes, and G. Bahl, Nature **555**, 346 (2018).

22   S. Liu, S. Ma, Q. Zhang, L. Zhang, C. Yang, O. You, W. Gao, Y. Xiang, T. J. Cui, and S. Zhang, Light Sci. Appl. **9**, 145 (2020).

23   H. Xue, Y. Yang, F. Gao, Y. Chong, and B. Zhang, Nat. Mater. **18**, 108 (2019).

24   X. Ni, M. Weiner, A. Alù, and A. B. Khanikaev, Nat. Mater. **18**, 113 (2019).

25   J. Hu, S. Zhuang, and Y. Yang, Phys. Rev. Lett. **132**, 213801 (2024).

26   Y.-L. Tao, J.-H. Wang, and Y. Xu, arXiv: 2307.00486.

27   P. Lai, J. Wu, Z. Pu, Q. Zhou, J. Lu, H. Liu, W. Deng, H. Cheng, S. Chen, and Z. Liu, Phys. Rev. Appl. **21**, 044002 (2024).

28   M. A. Nielsen, and I. L. Chuang, *Quantum Computation and Quantum Information* (Cambridge University Press, Cambridge, UK, 2010).

29   A. Einstein, B. Podolsky, and N. Rosen, Phys. Rev. **47**, 777 (1935).

30   M. D. Reid, P. D. Drummond, W. P. Bowen, E. G. Cavalcanti, P. K. Lam, H. A. Bachor, U. L. Andersen, and G. Leuchs, Rev. Mod. Phys. **81**, 1727 (2009).

31   C. H. Bennett, and S. J. Wiesner, Phys. Rev. Lett. **69**, 2881 (1992).

32   C. H. Bennett, G. Brassard, C. Crépeau, R. Jozsa, A. Peres, and W. K. Wootters, Phys. Rev. Lett. **70**, 1895 (1993).

33   D. Bouwmeester, J. W. Pan, K. Mattle, M. Eibl, H. Weinfurter, and A. Zeilinger, Nature **390**, 575 (1997).

34   B. Bradlyn, L. Elcoro, J. Cano, M. G. Vergniory, Z. Wang, C. Felser, M. I. Aroyo, and B. A. Bernevig, Nature **547**, 298 (2017).

35   M. Levin, and X. G. Wen, Phys. Rev. Lett. **96**, 110405 (2006).

36   A. Kitaev, and J. Preskill, Phys. Rev. Lett. **96**, 110404 (2006).

37   S. Ryu, and Y. Hatsugai, Phys. Rev. B **73**, 245115 (2006).

38   I. Peschel, J. Phys. A-Math. Gen. **36**, L205 (2003).

39   H. Li, and F. D. M. Haldane, Phys. Rev. Lett. **101**, 010504 (2008).

40   L. Fidkowski, Phys. Rev. Lett. **104**, 130502 (2010).

41   A. Chandran, M. Hermanns, N. Regnault, and B. A. Bernevig, Phys. Rev. B **84**, 205136 (2011).

42   X. L. Qi, H. Katsura, and A. W. W. Ludwig, Phys. Rev. Lett. **108**, 196402 (2012).

43   T. L. Hughes, E. Prodan, and B. A. Bernevig, Phys. Rev. B **83**, 245132 (2011).

44   A. Alexandradinata, T. L. Hughes, and B. A. Bernevig, Phys. Rev. B **84**, 195103 (2011).

45   C. Fang, M. J. Gilbert, and B. A. Bernevig, Phys. Rev. B **87**, 035119 (2013).

46   E. Prodan, T. L. Hughes, and B. A. Bernevig, Phys. Rev. Lett. **105**, 115501 (2010).

47   A. M. Turner, Y. Zhang, and A. Vishwanath, Phys. Rev. B **82**, 241102 (2010).

48   P. Zhu, K. Loehr, and T. L. Hughes, Phys. Rev. B **101**, 115140 (2020).

49   Q. Wang, D. Wang, and Q. H. Wang, EPL **124**, 50005 (2018).

50   T. Fukui, and Y. Hatsugai, Phys. Rev. B **98**, 035147 (2018).

51   Z. K. Lin, Y. Zhou, B. Jiang, B. Q. Wu, L. M. Chen, X. Y. Liu, L. W. Wang, P. Ye, and J. H. Jiang, Nat. Commun. **15**, 1601 (2024).

52   R. Islam, R. Ma, P. M. Preiss, M. Eric Tai, A. Lukin, M. Rispoli, and M. Greiner, Nature **528**, 77 (2015).

53   S. Yin, L. Ye, H. He, X. Huang, M. Ke, W. Deng, J. Lu, and Z. Liu, Sci. Bull. **69**, 1660 (2024).

54   H. Wu, H. He, L. Ye, J. Lu, M. Ke, W. Deng, and Z. Liu, Adv. Mater. **37**, 2500757 (2025).

55   H. Li, H. Chen, X. C. Sun, Y. B. Chen, C. He, and Y. F. Chen, Sci. China-Phys. Mech. Astron. **69**, 227013 (2026).

56   R. Thomale, D. P. Arovas, and B. A. Bernevig, Phys. Rev. Lett. **105**, 116805 (2010).

57   X. J. Yu, S. Yang, H. Q. Lin, and S. K. Jian, Phys. Rev. Lett. **133**, 026601 (2024).